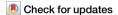
A Nature Portfolio journal



https://doi.org/10.1038/s43247-025-02396-w

Three-dimensional structure, crystallography, and magnetism of giant magnetofossils



Zhaowen Pei ^{1,2}, Emilie Ringe ^{3,4}, Liao Chang ¹ □, Richard J. Harrison⁴, Pengfei Xue ⁵ & Wyn Williams ²

Biomineralization has existed on Earth for billions of years, documenting life evolution history and major geological events. However, determining the origins of putative biogenic minerals remains a persistent challenge. A prime example is the micrometer-sized fossil magnetite crystals (giant magnetofossils) discovered in global marine sediments, dating from the present to 97 Ma ago. Their origin remains unclear because their shape and size are different from any known nanometer-sized magnetite produced by magnetotactic bacteria. Here, we present three-dimensional (3D) reconstructions of giant magnetofossils with nanometer resolution, and report two new morphologies of giant magnetofossils. By identifying diagnostic 3D morphological, crystallographic, and micromagnetic features, our results provide key identification criteria for giant magnetofossils and suggest a potential biologically controlled mineralization origin. This study provides a comprehensive 3D characterisation of giant magnetofossils, aiding the search for ancient microbial activities on Earth and extraterrestrial bodies.

Biominerals, formed through biomineralization by organisms, can be preserved as fossil records over billions of years, which provide critical insights into the life evolution and environmental conditions of ancient Earth^{1,2}. However, the biological origin of some biominerals has been strongly questioned due to the absence of co-preserved symbiotic organic components and well-defined modern analogs. For example, nanoscale magnetite crystals found in the Martian meteorite ALH84001, which exhibit similar morphological features to some modern magnetite magnetosomes, have caused substantial controversy regarding their origin³⁻⁶.

Magnetofossils, fossilized biogenic magnetite or greigite crystals preserved in sediments, are a well-established type of biomineral typically in the nanometer size range (~35–300 nm)⁷. They record key information about past microbial activity, geomagnetic field variations, and environmental changes^{7–10}. However, the discovery of anomalously large magnetofossil crystals (~0.5–4 μm) with peculiar morphology¹¹, presents an intriguing scientific mystery due to the absence of modern analogues. The first discovery of giant magnetofossils was reported in marine sediments from the Paleocene–Eocene Thermal Maximum (PETM) period at Ancora, New Jersey¹¹. Subsequent studies identified giant magnetofossils in the Pacific, Atlantic, and Indian Ocean sediments spanning from ~97 Ma to the present^{8,12–21}.

Giant magnetofossils have specific crystal shapes (e.g., spearhead, spindle, giant bullet, and needle), micrometer-sized dimensions, and high chemical purity and crystallographic perfection^{11,13}. The size and morphology of giant magnetofossil crystals are markedly distinct from conventional nanoscale magnetofossils produced by magnetotactic bacteria (MTB). Only giant bullets resemble conventional MTB-synthesized bulletshaped magnetofossils, yet are notably larger 13,16. Despite the presence of giant magnetofossils in modern marine sediments²⁰, no extant organisms are known to synthesize analogous minerals, rendering their biogenicity contentious. Moreover, the link between the occurrence of giant magnetofossils and past climate conditions remains controversial 11,13-21. Thus, searching for potential biogenic signatures of giant magnetofossils and organisms that produce these large magnetite crystals remains challenging. Further investigations are also needed to identify distinctive iron biomineralization processes and associated environmental conditions that these magnetofossils might exemplify.

Previous studies provide indirect evidence of a biological origin for giant magnetofossil crystals from crystal morphology, dimension distribution, chemical composition, and crystallography^{11,13,16,20,22}. However, these morphological and crystallographic studies relied on 2D microscopic observations of giant magnetofossils, with limited 3D characterizations

¹SKLab-DeepMinE, MOEKLab-OBCE, School of Earth and Space Sciences, Peking University, Beijing, China. ²School of GeoSciences, University of Edinburgh, Edinburgh, UK. ³Department of Materials Science and Metallurgy, University of Cambridge, Cambridge, UK. ⁴Department of Earth Sciences, University of Cambridge, Cambridge, UK. ⁵State Key Laboratory of Marine Geology, Tongji University, Shanghai, China. ⊠e-mail: liao.chang@pku.edu.cn

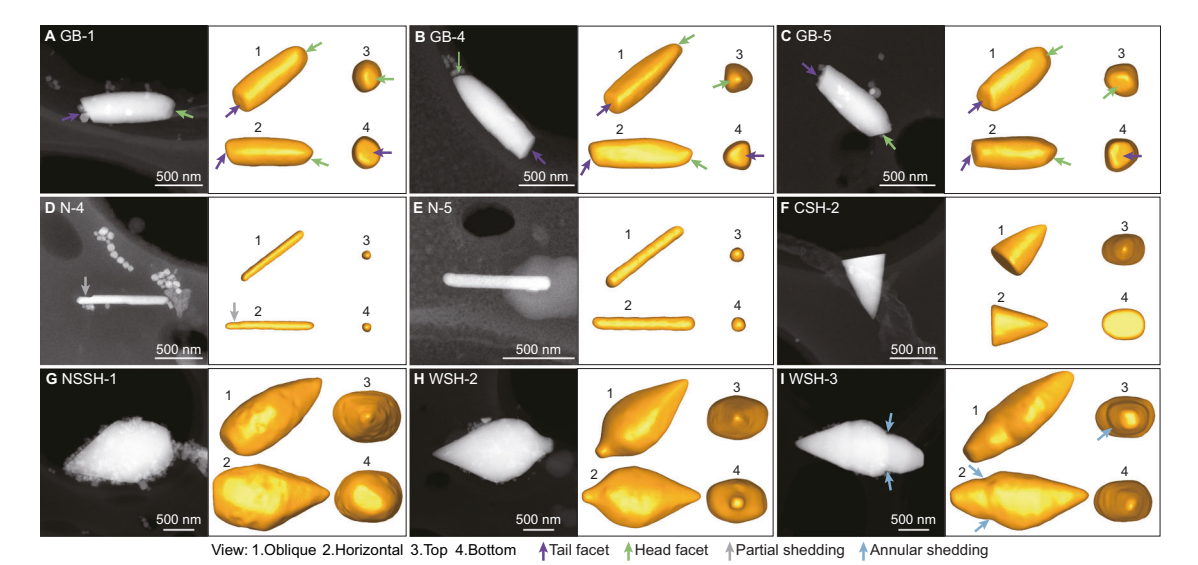


Fig. 1 | Electron tomography reconstruction results of single giant magnetofossil crystals. High-angle annular dark-field (HAADF) images of (A–C) giant bullet (GB), (D, E) needle (N), (F) cone spearhead (CSH), (G) no-stalk spearhead (NSSH), and (H, I) whole spearhead (WSH) particles (large bright particles) and four

different views of reconstructed particles in yellow (oblique, horizontal, top, and bottom). Colored arrows represent identified specific crystal planes and structures. More particle reconstruction results are provided in Supplementary Fig. S2.

achieved through scanning electron microscopy (SEM) for certain morphotypes^{8,11–23}. However, a complete 3D structural characterization remains essential for determining their diagnostic signatures.

In this study, we employed transmission electron microscope (TEM)-based electron tomography, electron diffraction, and finite element micromagnetic simulations to characterize giant magnetofossil crystals. We obtained 3D reconstructions of giant magnetofossils with nanometer resolution and identified two previously unreported morphologies of micrometer-sized fossil magnetite. We identified characteristic crystal planes of these magnetite crystals from tomographic reconstruction data using a 3D crystal plane cluster-analysis approach. Furthermore, we demonstrate that each type of giant magnetofossil exhibits a unique combination of 3D microstructures, crystallographic orientations, and magnetic properties. These findings suggest a potential iron biomineralization origin of giant magnetofossils.

Results

3D morphology of single giant magnetofossil crystals

We obtained the 3D structures of more than 20 particles, including giant bullets, needles, and spearheads, using electron tomography with nanoscale resolution (Fig. 1). No suitable spindle-shaped magnetofossils were found in these samples. Reconstructed giant bullets have lengths of ~500-1000 nm with widths of ~200-450 nm (Supplementary Fig. S1; Supplementary Table S1). The longitudinal sections of giant bullet-shaped particles have approximately polygonal cross sections, possibly hexagonal or octagonal (Fig. 1A-C; Supplementary Figs. S2A-D and S3). These polygonal crosssections and 3D structures indicate the presence of faceted rather than smooth curved surfaces. In particular, both the 2D images and the 3D reconstructions reveal that most giant bullet crystals have pronounced truncated planes at both ends (Fig. 1A-C; Supplementary Fig. S2A-D). Reconstructed needles have high aspect ratios, with lengths of ~500-1000 nm and widths of ~100 nm (Supplementary Fig. S1; Supplementary Table S1). The needles have polyhedral lateral surfaces with approximately hexagonal cross-sections (Fig. 1D, E; Supplementary Figs S2E-G and S3). The needles also have a series of distinct and asymmetric truncated crystal planes at both ends (Fig. 1D, E; Supplementary Fig. S2E-G). A needle particle appears to have a broken end, indicating possible partial shedding (Fig. 1D). We have reconstructed three types of spearheads²⁰: cone spearhead (Fig. 1F; Supplementary Fig. S2H), no-stalk spearhead (Fig. 1G), and whole spearhead (Fig. 1H, I; Supplementary

Fig. S2I). The lengths of cone spearheads are 600-800 nm, while the lengths of the other two types of spearheads reach $1.5-2.5\,\mu m$ (Supplementary Fig. S1; Supplementary Table S1). All three types of spearheads have a sharp tip and elongated hexagon-shaped cross-sections with particle widths greater than heights (Fig. 1F–I; Supplementary Fig. S2H, I). A whole spearhead particle has an incomplete middle section, likely associated with annular shedding (Fig. 1I).

Discovery of kinked giant bullet-shaped and sock-shaped magnetofossils

We have discovered two previously unreported giant magnetofossil particle forms. One is bullet-shaped particle with a relatively pointed head and a kinked tail (Fig. 2A, B), hereby referred to as kinked giant bullets. Their lengths range between 1.1–1.2 μm , with widths and heights of ~200–350 nm, and axial ratios higher than typical giant bullet particles (Fig. 2D; Supplementary Fig. S1; Supplementary Table S1). The other identified particle form is a unique sock-like particle, characterized by a tilted head with a truncated flat plane on one side and a truncated flat tail, hereby referred to as sock (Fig. 2C). Its dimensions are ~2 μm in length and ~700 nm for both width and height (Supplementary Table S1).

Crystallography of giant magnetofossils

Selected-area electron diffraction (SAED) and high-resolution TEM (HRTEM) imaging of most giant magnetofossils confirm perfect crystallinity and main crystal planes {111}, {100}, {110}, and {311} of magnetite (Fig. 3; Supplementary Fig. S4). We also analyzed previous results to synthesize data on the crystallographic direction corresponding to the long axis of each giant magnetofossil particle (Table 1). Most giant bullet particles (5 out of 6) have long axes parallel to [111] (Fig. 3A; Table 1; Supplementary Fig. S4A), whereas only one particle aligns with [110] (Supplementary Fig. S4B). Long axes of all analyzed needle particles (11 in total) are approximately parallel to [111] (Fig. 3B; Table 1; Supplementary Fig. S4C-G). Long axes of all cone and no-stalk spearheads (2 out of 2) are parallel to [311] (Fig. 3C; Table 1). Most whole spearheads (3 out of 4) have long axes parallel to [110] (Fig. 3D; Table 1), whereas the long axis orientation of the fourth particle remains indeterminate based on the available published data (20). Spindle particles (2 out of 2) also have long axes parallel to [110] (Table 1; Supplementary Fig. S4H).

We proposed a quantitative approach to utilize clustering and orientation analysis of surface mesh normal vectors in reconstructed particles,

Fig. 2 | Electron tomography reconstruction results of single giant magnetofossil crystals. High-angle annular dark-field (HAADF) images of (A, B) a kinked giant bullet (KGB) and (C) a sock-shaped particle (large bright particles) and four different views of reconstructed particles in yellow (oblique, horizontal, top, and bottom). Green arrows represent kinked tails in the particles. D The length and width of all reconstructed giant magne-

tofossil particles (colored circles) and small kinked bullet particles synthesized by magnetotactic bac-

teria (black circles)²⁶⁻²⁸.

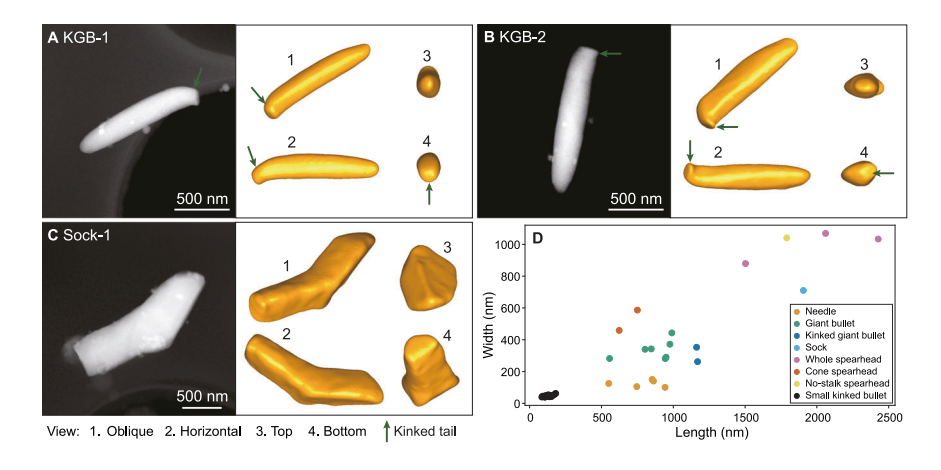
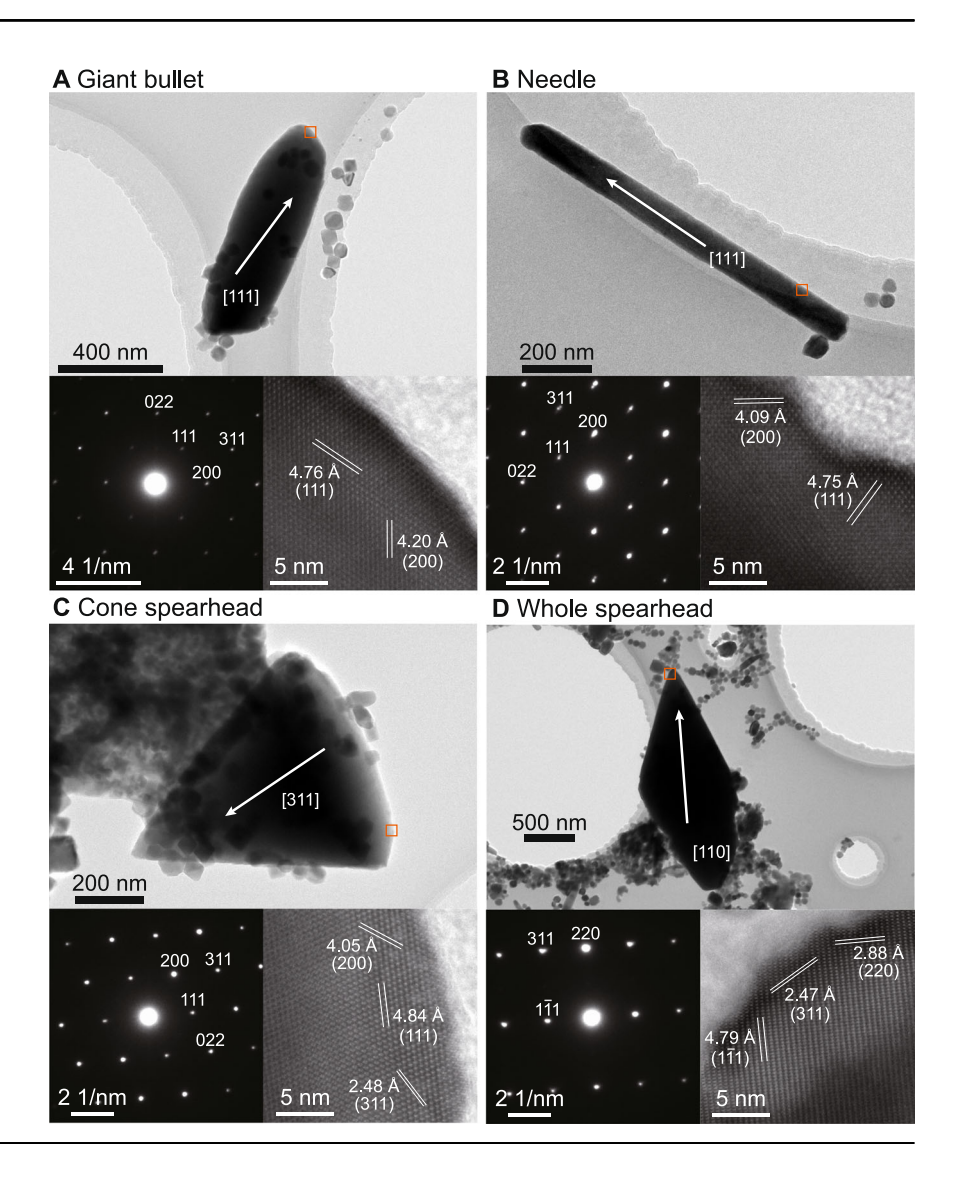


Fig. 3 | Transmission electron microscope (TEM) analyses of single giant magnetofossil crystals.

A–D Bright-field TEM images, with selected-area electron diffraction (SAED) patterns, and high-resolution transmission electron microscopy (HRTEM) images shown below each TEM image. Orange boxes represent the location for HRTEM imaging. White arrows indicate the particle elongation direction marked with crystallographic lattice direction. White solid lines mark primary lattice fringes marked with corresponding d-spacing and Miller indices (hkl). More SAED and HRTEM analyses are provided in Supplementary Fig. S4.



which enables the identification of a series of characteristic crystal planes for each type of giant magnetofossils (Fig. 4; Supplementary Fig. S5). Our clustering analysis of surface mesh normal vectors indicate that the truncated planes at both tails and heads of most giant bullet magnetofossils, and the lateral crystal planes of giant bullets and needles are all consistently {110} (Fig. 4A–E; Supplementary Fig. S5A–G). Multiple {311} crystal facets in all three types of spearheads are identified (Fig. 4F–I; Supplementary Fig. S5H), consistent with the proposed crystallographic model of spearheads¹¹.

Micromagnetic simulation of giant magnetofossils

Saturation isothermal remanent magnetization (SIRM) domain states were calculated in twenty external magnetic field directions (Fig. 5; Supplementary Figs. S6 and S7; Tables S2 and S3). In twenty external field directions, the proportion of SIRM state types is related to the morphology of giant magnetofossils (Supplementary Table S3): needles and kinked giant bullets are mainly in single domain (SD) states; giant bullets, cone spearheads, and no-stalk spearheads are mainly in single vortex (SV) states; whole spearheads

Table 1 | Long-axis crystallographic directions of different types of giant magnetofossil crystals

Туре	Long-axis direction	Match count / total instances ^a
Giant bullet	[111]	5/6
Needle	[111]	11/11
Whole spearhead	[110]	3/4
Cone and no-stalk spearhead	[311]	2/2
Spindle	[110]	2/2

^aCrystallographic direction analyses can be found in Fig. 3 and Supplementary Fig. S4, as well as previous studies ^{11,16,20}.

and the sock particle exhibit similar proportions of SV and multiple vortex (MV) states. SIRM states with lowest total magnetic energy also vary with the morphology: giant bullets are primarily in SV states (Fig. 5A, B; Supplementary Fig. S8A–E); kinked giant bullets show SV states (Fig. 5C; Supplementary Fig. S8F); needles typically exhibit SD states (Fig. 5D, E; Supplementary Fig. S8G–I); spearheads and sock-shaped particle exhibit a range of complex SV to MV states depending on their size and shape (Fig. 5F–J; Supplementary Fig. S8J, K). SIRM direction distributions in twenty external fields become less concentrated from needles, kinked giant bullets, giant bullets, to spearheads and the sock (Fig. 5K). Micromagnetic simulations of single giant magnetofossil crystals show a general reduction in average coercivity (B_c) and the ratio of saturation remanence to saturation magnetization (M_{rs}/M_s) from needles, kinked giant bullets, giant bullets, to spearheads and the sock, corresponding to a progressive descent towards the lower left on the Néel diagram (Fig. 5L and Supplementary Fig. S9)²⁴.

Discussion

3D reconstruction shows that multiple giant magnetofossil particles from the same category have relatively consistent characteristic 3D morphological, structural, and crystallographic features. The primary crystal planes of giant bullets, needles, and spearheads are polyhedral rather than smoothly curved (Fig. 1; Supplementary Figs. S2, S3). We have identified distinctive truncated {110} facets at the head and tail of giant bullets (Figs. 1A-C, 4A-C; Supplementary Figs. S2A-D, S5A-D) and asymmetric facets at both ends of needles (Fig. 1D, E; Supplementary Fig. S2E-G). Kinked giant bullets and the sock particle are characterized by a kinked tail and head, respectively (Fig. 2A-C). Moreover, giant bullets, kinked giant bullets, and needles exhibit similar width and height, making them approximately uniaxial particles, while the three axes of spearheads have different dimensions (Fig. 1; Supplementary Fig. S1; Supplementary Table S1). Combining previous results with our data, we have identified consistent long-axis crystallographic orientations for each type of giant magnetofossil particle: giant bullets and needles elongate along the [111], whole spearheads and spindles elongate along [110], and cone and no-stalk spearheads elongate along [311] (Fig. 3; Table 1; Supplementary Fig. S4). Characteristic {110} planes in giant bullets and needles, and {311} planes in spearheads were also recognized (Fig. 4; Supplementary Fig. S5). The consistent 3D diagnostic signatures across diverse particles within each giant magnetofossil category provide robust criteria for their identification in natural materials. This morphological uniformity, which is difficult to produce through abiogenic processes, likely suggests biologically controlled mineralization and serves as a potential biomarker.

The morphologies of giant bullets resemble conventional bullet-shaped magnetofossils produced by magnetotactic bacteria (MTB), supporting the hypothesis of their biological origins^{13,17}. However, apart from the size difference, MTB-synthesized bullet crystals predominantly have [100] and [110] long-axis orientations^{25–28}, unlike the [111] elongation of giant bullets (Table 1). Additionally, conventional bullets lack the distinct {110} facets at both ends seen in giant bullets. Kinked giant bullets and the sock particle (Fig. 2A–C) have similar morphology to some kinked bullet-shaped

magnetite crystals synthesized by MTB, such as AV-1, LO-1, HSMV-1 26 , MYR-1 25,27 , and WYHR-1 28 suggesting a possible biogenic origin, despite their notable size discrepancy (~1.1 μm for kinked giant bullets, ~2 μm for the sock crystal, and <300 nm for MTB-synthesized magnetite) (Fig. 2D). To date, only one MTB species was found to be capable of producing needle-shaped magnetite of about 300 nm long 29 —smaller than needle crystals (~500–1000 nm) typically found in geological records. Moreover, the elongated prismatic magnetite particles typically have a long-axis orientation along [111] 28 , yet their dimensions and aspect ratios are notably smaller than needle magnetofossils.

It was found that gene networks control the morphology of magnetite magnetosomes in MTB, implying that crystal morphology could be a proxy for ancient MTB taxonomy ^{28,30}. In contrast to smaller conventional bullet crystals ²⁸, giant bullets are larger with distinct 3D morphological and crystallographic features. Kinked giant bullets and the sock particle are also larger than conventional kinked bullets. Despite having similar cross-sectional and structural features, whole spearheads and potentially partial spearheads (cone and no-stalk spearheads) have different long-axis orientations. If these giant magnetite crystals are all biogenic, these variations in dimension, morphology, and crystallography may indicate that these bulletshaped (giant bullets, kinked giant bullets, the sock particle, and conventional bullets and kinked bullets) and spearhead-shaped (whole, cone, and no-stalk spearheads) magnetite crystals could originate from distinct biological species.

Magnetic characteristics play a crucial role in detecting giant magnetofossils in natural samples. It has been suggested that needles can be detected using high-resolution first-order reversal curve (FORC) measurements due to their extreme elongations¹⁴. Our simulation results provide a numerical reference range for hysteresis parameters such as coercivity (Fig. 5L), supporting the interpretation of rock magnetic signals of giant magnetofossils. However, simulation results also reveal that some types of giant magnetofossil crystal have intricate magnetic domains and characteristic magnetic parameter range, controlled by their size and shape (Fig. 5). Magnetic hysteresis properties of giant magnetofossils were analyzed in the context of published data for different magnetite types (MTBsynthesized, extracellularly synthesized, and chemically synthesized)^{8,25,31–52} using the Néel diagram (Fig. 5L)²⁴. Needle-shaped crystals show parameter ranges overlapping with bullet-shaped magnetosomes^{25,41}, while kinked giant bullets exhibit close similarity to cuboctahedral and prismatic magnetosomes³¹⁻⁴¹. Notably, giant bullet-, spearhead-, and sock-shaped magnetite crystals form a distinct cluster in the lower-left region (i.e., $B_{\rm c}$ < 10 mT, $M_{\rm rs}/M_{\rm s}$ < 0.1). This cluster differs markedly from MTB-derived magnetosomes/magnetofossils^{8,31-45}, but rather aligns closely with some extracellularly and chemically synthesized magnetite samples^{32,46–52}. These findings expand the known range of magnetic signatures associated with potentially biogenic magnetite. Therefore, given the typically low abundance of giant magnetofossils in natural samples, along with the complex magnetic behavior, their detection solely based on magnetic properties poses a substantial challenge.

The biological functions of giant magnetite crystals remain undetermined^{11,13}, with current hypotheses including magnetoreception¹³, structural reinforcement in hard tissues⁵³, and other potential biological roles. The SD state of needles implies their potential for high magnetic navigation efficiency. The complex and chaotic vortex states of giant bullets and spearheads, coupled with the misalignment between the long-axis and the magnetic easy axis of spearheads, suggest that they may not fully maximize their magnetic moments for effective magnetic alignment. Moreover, previous micromagnetic simulations have shown that micronsized magnetite magnetofossils, when arranged in chains, retain sufficient magnetotaxis efficiency⁵⁴. Consequently, investigating whether these giant magnetite crystals can be arranged into chains in modern organisms is crucial for elucidating their biological functions.

Our study reveals 3D structural and crystallographic signatures of giant magnetofossils, which serve as diagnostic criteria for their identification and potential biosignatures in geological records. It is essential to search for

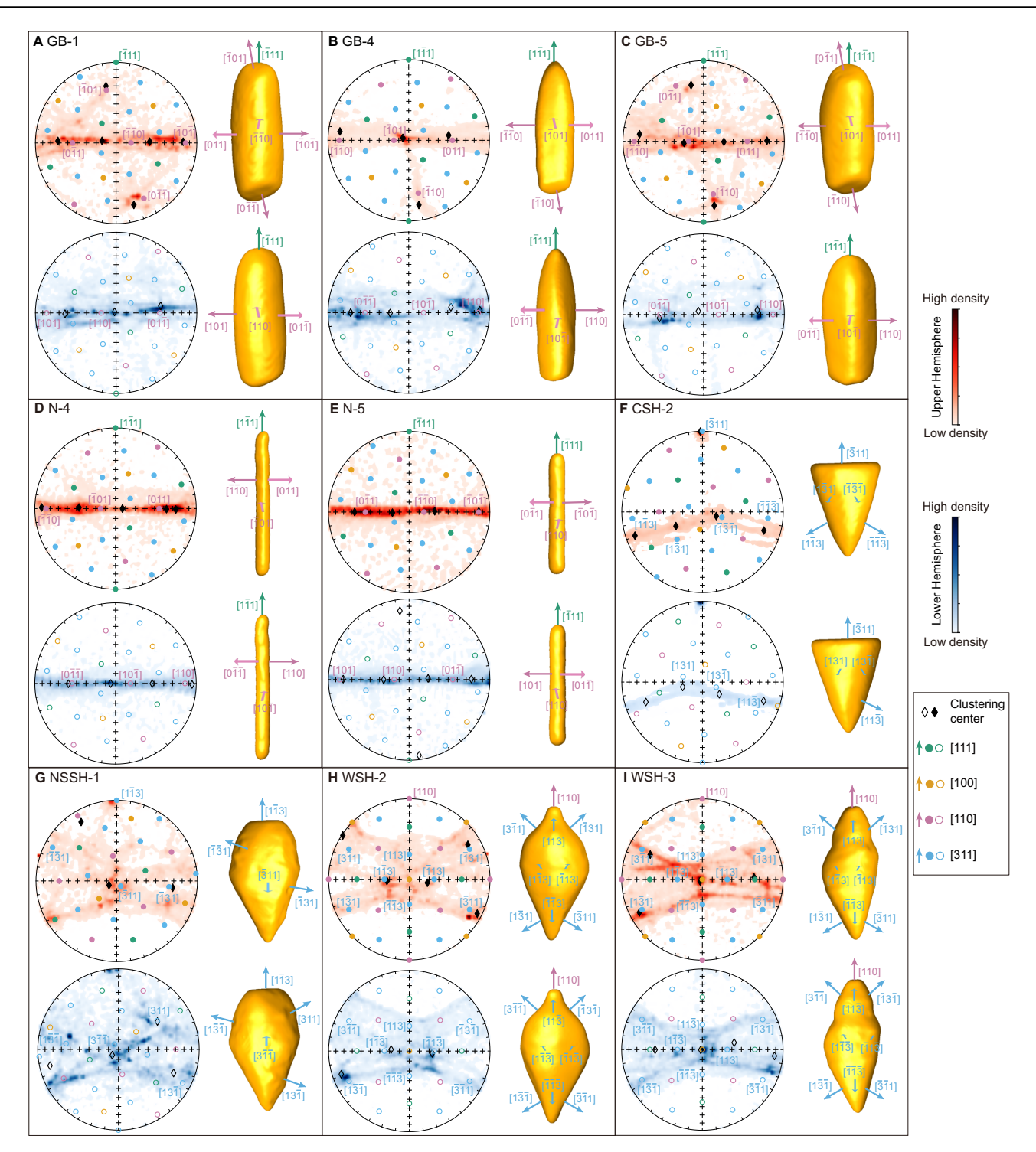


Fig. 4 | Crystal plane clustering and orientation analysis of reconstructed single giant magnetofossil particles. Stereographic projection of all normal vectors of surface meshes for reconstructed giant magnetofossil crystals, colored in yellow of (A–C) giant bullet (GB), (D, E) needle (N), (F) cone spearhead (CSH), (G) no-stalk spearhead (NSSH), and (H, I) whole spearhead (WSH) particles. K-means clustering centers of normal vectors, and theoretical crystal plane groups determined by the known long-axis direction, including {111}, {100}, {110}, and {311}, are also marked

correspondingly. Red and blue contours represent normal vector distributions on the upper and lower hemispheres, respectively, with corresponding particle meshes on the right. Black solid and hollow diamonds represent clustering centers. Colored solid and hollow circles represent theoretical crystal planes. Colored arrows represent normal vectors of theoretical crystal planes. More clustering and orientation analyses are provided in Supplementary Fig. S5.

modern organisms that produce giant magnetite crystals, important for conclusively determining their biological origin and function. Furthermore, advanced geochemical analyses, including atom probe tomography for detecting organic elements within particles⁵⁵, characteristic isotope signals from biologically controlled processes¹¹, and in situ observations of

potentially co-preserved organic materials, hold promise for future investigations. These 3D morphological, crystallographic, and chemical characterization approaches are crucial for identifying biogenic minerals and searching for potential biosignatures on ancient Earth and extraterrestrial bodies.

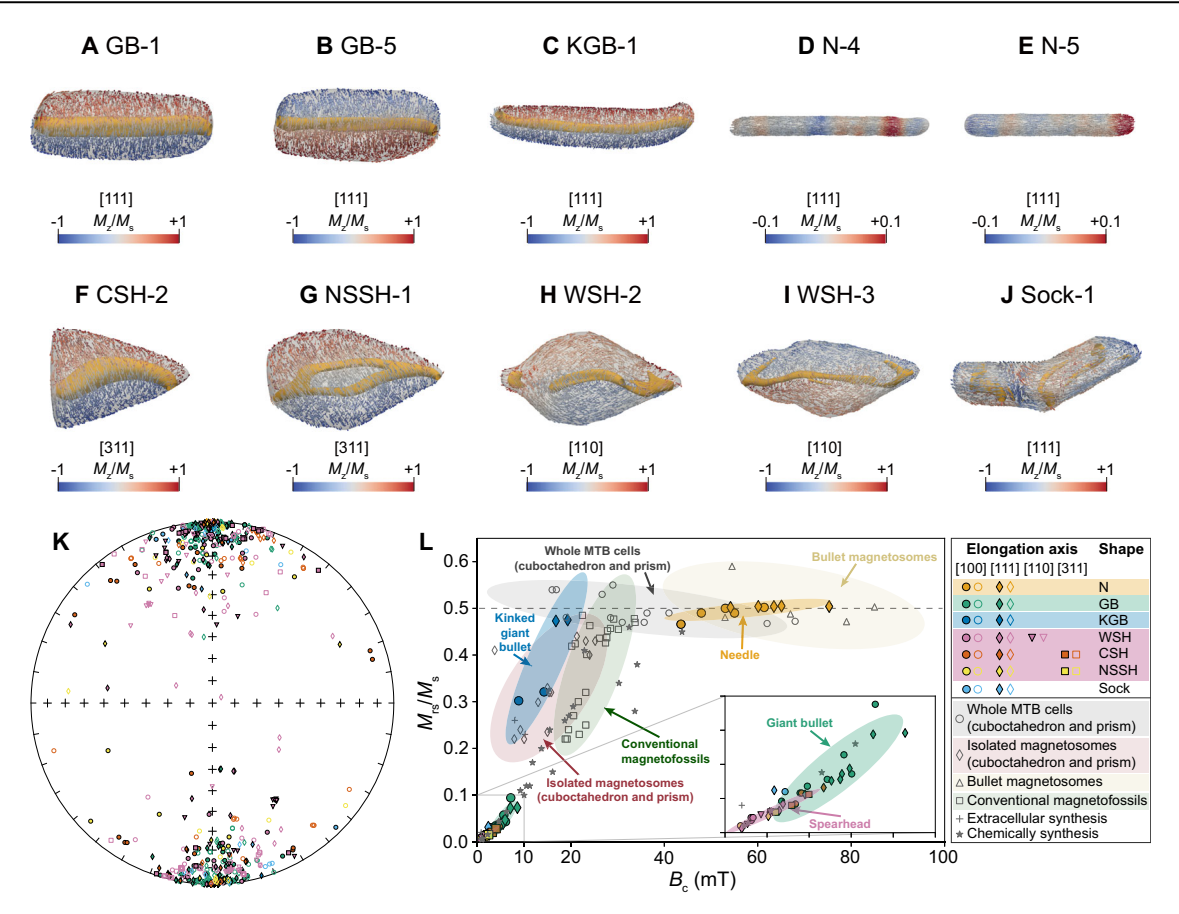


Fig. 5 | Micromagnetic simulation results of reconstructed single giant magnetofossil particles. A–J Selected modeled saturation isothermal remanent magnetization (SIRM) domain states with the lowest total magnetic energy of giant bullets, kinked giant bullets, needles, spearheads, and the sock-shaped crystal, with corresponding applied field directions provided in Supplementary Table S2 and S3. Arrows represent magnetic moment directions. Arrows are colored by the normalized magnetization in the direction perpendicular to the page. Vortex cores are colored orange. More simulated SIRM domain states are provided in Supplementary Fig. S8. K Stereographic projection of SIRM state directions in twenty external magnetic field directions. L The Néel diagram shows coercivity (B_c) versus the ratio of saturation remanence to saturation magnetization ($M_{\rm rs}/M_{\rm s}$) of each reconstructed particle for needles (N), kinked giant bullets (KGB), giant bullets (GB), cone

spearheads (CSH), no-stalk spearheads (NSSH), whole spearheads (WSH), and the sock-shaped crystal (sock). Colored circles, diamonds, downward-pointing triangles, and squares represent simulation results of different crystal elongation axes. Solid and hollow symbols denote SIRM directions onto the upper and lower hemispheres, respectively. Dark gray markers represent the hysteresis parameters of whole magnetotactic bacteria (MTB) cells (cuboctahedron and prism magnetite crystals; circles)³¹⁻⁴¹, isolated magnetosomes (cuboctahedron and prism magnetite crystals; diamonds)^{31,36,41}, bullet-shaped magnetosomes (upward-pointing triangles)^{25,41}, conventional magnetofossils (squares)^{8,42-45}, extracellularly synthesized magnetite (crosses)^{32,46,47}, and chemically synthesized magnetite (pentagrams)⁴⁸⁻⁵². 95% confidence ellipses for the hysteresis data of typical magnetite categories are provided.

Materials and methods Sample preparation

The marine sediment samples analyzed in this study were obtained from the International Ocean Discovery Program (IODP). Detailed information regarding the sites and stratigraphic positions is provided in Supplementary text. We selected TEM copper grids containing typical giant magnetofossils from our previous studies ^{16,20} for subsequent TEM observations and electron tomography.

TEM observations

Sample copper grids were utilized for TEM analysis using a JEOL JEM-2100 TEM at the Institute of Geology and Geophysics, Chinese Academy of Sciences (IGGCAS) in Beijing, operating at a voltage of 200 kV. Bright-field TEM imaging, SAED analysis, and HRTEM imaging were performed. We have conducted crystallographic orientation and Miller index analysis on SAED and HRTEM images, and collected data from previous studies 11,16,20 for data synthesis (Supplementary text).

Electron tomography

Sample copper grids were utilized for electron tomography using a FEI Krios TEM operating at 300 kV and 80 K at the Wolfson Electron Microscopy

Suite, University of Cambridge. The sample was tilted between $\pm 65^{\circ}$ and $\pm 70^{\circ}$ with steps of 1° or 1.5°, and multiple high-angle annular dark-field (HAADF) images were captured. A compressed sensing reconstruction algorithm⁵⁶ was used for 3D tomography reconstruction. Reconstruction results were segmented with Dragonfly software version 2022.2⁵⁷ to generate particle surface meshes. More details on the tomography analysis are provided in Supplementary text.

Crystal plane clustering and determining

Normal vectors of reconstructed surface meshes were extracted for k-means clustering analysis to identify potential crystal planes. The crystallographic orientation of the particle's long-axis was confirmed through SAED and HRTEM analysis. Given the multiplicity of potential orientations for crystal long axis, we proposed a quantitative approach to identify the ideal crystal plane group (from {111}, {100}, {110}, and {311}) that best fits all cluster centers. The angular difference between each cluster center and the closest plane in each ideal crystal plane group was calculated at different possible long-axis orientations. The long-axis orientation corresponding to the ideal crystal plane group with the smallest total angular difference was chosen for subsequent plane analysis. More details on the crystal plane analysis are provided in Supplementary text.

Micromagnetic simulation

Based on the reconstructed particle with realistic 3D shapes from electron tomography, we have established geometric models with volume meshing using the Coreform Cubit software version 2023.8⁵⁸. Subsequently, the finite element micromagnetic simulation software MERRILL version 1.8.6 was used to run micromagnetic simulations⁵⁹, calculating the hysteresis loops of each particle in twenty uniformly distributed directions on the sphere (Supplementary Table S2). Combining crystallographic observations, we considered four types of magnetite magnetocrystalline anisotropy configurations, aligning the long-axis of reconstructed particles respectively along: the magnetic easy axis [111] and the magnetic hard axis [100] for all particles; [311] specifically for cone and no-stalk spearheads; [110] specifically for whole spearheads. ParaView software version 5.11.2⁶⁰ was used for domain state visualization. More details on the micromagnetic calculations are provided in Supplementary text.

Data availability

Mesh files and movie files of all reconstructed particles, micromagnetic simulation output files, and data for Figs. 2D and 5L are available at the Zenodo repository 61 .

Code availability

Crystal plane analysis code is available at the Zenodo repository⁶¹.

Received: 26 January 2025; Accepted: 16 May 2025; Published online: 24 May 2025

References

- Weiner, S. & Dove, P. M. An overview of biomineralization processes and the problem of the vital effect. *Rev. Mineral. Geochem.* 54, 1–29 (2003).
- Pérez-Huerta, A., Coronado, I. & Hegna, T. A. Understanding biomineralization in the fossil record. *Earth-Sci. Rev.* 179, 95–122 (2018).
- McKay, D. S. et al. Search for past life on Mars; possible relic biogenic activity in martian meteorite ALH84001. Science 273, 924–930 (1996).
- Buseck, P. R. et al. Magnetite morphology and life on Mars. Proc. Natl. Acad. Sci. USA 98. 13490–13495 (2001).
- Golden, D. C. et al. Evidence for exclusively inorganic formation of magnetite in martian meteorite ALH84001. *Am. Mineral.* 89, 681–695 (2004).
- Thomas-Keprta, K. L., Clemett, S. J., McKay, D. S., Gibson, E. K. & Wentworth, S. J. Origins of magnetite nanocrystals in martian meteorite ALH84001. *Geochim. Cosmochim. Acta* 73, 6631–6677 (2009).
- Kopp, R. E. & Kirschvink, J. L. The identification and biogeochemical interpretation of fossil magnetotactic bacteria. *Earth-Sci. Rev.* 86, 42–61 (2008).
- Chang, L. et al. Coupled microbial bloom and oxygenation decline recorded by magnetofossils during the Palaeocene-Eocene thermal maximum. *Nat. Commun.* 9, 4007 (2018).
- Chang, L. et al. Indian Ocean glacial deoxygenation and respired carbon accumulation during mid-late Quaternary ice ages. *Nat. Commun.* 14, 4841 (2023).
- Slotznick, S. P., Egli, R. & Lascu, I. Magnetofossils: relicts and records of deep time and space. *Elements* 19, 215–221 (2023).
- Schumann, D. et al. Gigantism in unique biogenic magnetite at the Paleocene-Eocene Thermal Maximum. *Proc. Natl. Acad. Sci. USA* 105, 17648–17653 (2008).
- Kopp, R. E. et al. An Appalachian Amazon? Magnetofossil evidence for the development of a tropical river-like system in the mid-Atlantic United States during the Paleocene-Eocene thermal maximum. Paleoceanography 24, PA4211 (2009).
- Chang, L. et al. Giant magnetofossils and hyperthermal events. *Earth Planet. Sci. Lett.* 351–352, 258–269 (2012).

- Wagner, C. L. et al. In situ magnetic identification of giant, needleshaped magnetofossils in Paleocene-Eocene Thermal Maximum sediments. *Proc. Natl. Acad. Sci. USA* 118, e2018169118 (2021).
- Wagner, C. L. et al. Diversification of iron-biomineralizing organisms during the Paleocene-Eocene Thermal Maximum: evidence from quantitative unmixing of magnetic signatures of conventional and giant magnetofossils. *Paleoceanogr. Paleoclimatol.* 36, e2021PA004225 (2021).
- Xue, P., Chang, L., Pei, Z. & Harrison, R. J. Discovery of giant magnetofossils within and outside of the Palaeocene-Eocene thermal maximum in the North Atlantic. *Earth Planet. Sci. Lett.* 584, 117417 (2022).
- Xue, P., Chang, L., Dickens, G. R. & Thomas, E. A depth-transect of ocean deoxygenation during the Paleocene-Eocene thermal maximum: Magnetofossils in sediment cores from the Southeast Atlantic. J. Geophys. Res.: Solid Earth 127, e2022JB024714 (2022).
- Wagner, C. L., Stassen, P., Thomas, E., Lippert, P. C. & Lascu, I. Magnetofossils and benthic foraminifera record changes in food supply and deoxygenation of the coastal marine seafloor during the Paleocene-Eocene Thermal Maximum. *Paleoceanogr. Paleoclimatol.* 37, e2022PA004502 (2022).
- 19. Kadam, N. et al. Discovery of late Quaternary giant magnetofossils in the Bay of Bengal. *Commun. Earth. Environ.* **5**, 107 (2024).
- Xue, P. & Chang, L. Spatiotemporal distribution of giant magnetofossils holds clues to their biological origin. *Geology* 52, 453–457 (2024).
- Wagner, C. L. et al. Discovery of giant and conventional magnetofossils bookending Cretaceous Oceanic Anoxic Event 2. Commun. Earth. Environ. 5, 386 (2024).
- Wang, H., Wang, J., Chen-Wiegart, Y. C. & Kent, D. V. Quantified abundance of magnetofossils at the Paleocene-Eocene boundary from synchrotron-based transmission X-ray microscopy. *Proc. Natl. Acad. Sci. USA* 112, 12598–12603 (2015).
- 23. Kirschvink, J. L. Radio waves zap the biomagnetic compass. *Nature* **509**, 296–297 (2014).
- Néel, L. Some theoretical aspects of rock-magnetism. Adv. Phys. 4, 191–243 (1955).
- Li, J. et al. Biomineralization, crystallography and magnetic properties of bullet-shaped magnetite magnetosomes in giant rod magnetotactic bacteria. Earth Planet. Sci. Lett. 293, 368–376 (2010).
- Lefèvre, C. T. et al. Morphological features of elongated-anisotropic magnetosome crystals in magnetotactic bacteria of the *Nitrospirae* phylum and the *Deltaproteobacteria* class. *Earth Planet. Sci. Lett.* 312, 194–200 (2011).
- Li, J. et al. Crystal growth of bullet-shaped magnetite in magnetotactic bacteria of the *Nitrospirae* phylum. *J. R. Soc. Interface* 12, 20141288 (2015).
- Li, J. et al. Bullet-shaped magnetite biomineralization within a magnetotactic Deltaproteobacterium: Implications for magnetofossil identification. J. Geophys. Res. Biogeosci. 125, e2020JG005680 (2020).
- Vali, H. & Kirschvink, J. L. Observations of magnetosome organization, surface structure, and iron biomineralization of undescribed magnetic bacteria: environmental speculations, in Iron Biominerals, R. B. Frankel, R. P. Blakemore, Eds. (Springer, US, 1990), pp. 97–115.
- Liu, P. et al. Key gene networks that control magnetosome biomineralization in magnetotactic bacteria. Natl. Sci. Rev. 10, nwac238 (2023).
- Moskowitz, B. M., Frankel, R. B., Flanders, P. J., Blakemore, R. P. & Schwartz, B. B. Magnetic properties of magnetotactic bacteria. *J. Magn. Magn. Mater.* 73, 273–288 (1988).
- Moskowitz, B. M., Frankel, R. B., Bazylinski, D. A., Jannasch, H. W. & Lovley, D. R. A comparison of magnetite particles produced anaerobically by magnetotactic and dissimilatory iron-reducing bacteria. *Geophys. Res. Lett.* 16, 665–668 (1989).

- Moskowitz, B. M., Frankel, R. B. & Bazylinski, D. A. Rock magnetic criteria for the detection of biogenic magnetite. *Earth Planet. Sci. Lett.* 120, 283–300 (1993).
- Lin, W. & Pan, Y. Uncultivated magnetotactic cocci from Yuandadu park in Beijing, China. Appl. Environ. Microbiol. 75, 4046–4052 (2009).
- Zhu, K. et al. Isolation and characterization of a marine magnetotactic spirillum axenic culture QH-2 from an intertidal zone of the China Sea. Res. Microbiol. 161, 276–283 (2010).
- Li, J., Wu, W., Liu, Q., & Pan, Y. Magnetic anisotropy, magnetostatic interactions and identification of magnetofossils. *Geochem. Geophys. Geosyst.* 13 (2012).
- Jovane, L., Florindo, F., Bazylinski, D. A. & Lins, U. Prismatic magnetite magnetosomes from cultivated M agnetovibrio blakemorei strain MV-1: a magnetic fingerprint in marine sediments?. *Environ. Microbiol. Rep.* 4, 664–668 (2012).
- Katzmann, E. et al. Analysis of magnetosome chains in magnetotactic bacteria by magnetic measurements and automated image analysis of electron micrographs. *Appl. Environ. Microbiol.* 79, 7755–7762 (2013).
- Wang, Y. et al. Characterizing and optimizing magnetosome production of Magnetospirillum sp. XM-1 isolated from Xi'an City Moat, China. FEMS Microbiol. Lett. 362, fnv167 (2015).
- Li, J. et al. Biomineralization and magnetism of uncultured magnetotactic coccus strain THC-1 with non-chained magnetosomal magnetite nanoparticles. J. Geophys. Res. Solid Earth 125, e2020JB020853 (2020).
- Pei, Z., Chang, L., Bai, F. & Harrison, R. J. Micromagnetic calculation of the magnetite magnetosomal morphology control of magnetism in magnetotactic bacteria. J. R. Soc. Interface 20, 20230297 (2023).
- Pan, Y. et al. The detection of bacterial magnetite in recent sediments of Lake Chiemsee (southern Germany). Earth Planet. Sci. Lett. 232, 109–123 (2005).
- Roberts, A. P. et al. Magnetotactic bacterial abundance in pelagic marine environments is limited by organic carbon flux and availability of dissolved iron. *Earth Planet. Sci. Lett.* 310, 441–452 (2011).
- 44. Ludwig, P. et al. Characterization of primary and secondary magnetite in marine sediment by combining chemical and magnetic unmixing techniques. *Glob. Planet. Change* **110**, 321–339 (2013).
- Liu, S. et al. Insolation driven biomagnetic response to the Holocene Warm Period in semi-arid East Asia. Sci. Rep. 5, 8001 (2015).
- Vali, H. et al. Formation of tabular single-domain magnetite induced by Geobacter metallireducens GS-15. Proc. Natl. Acad. Sci. USA 101, 16121–16126 (2004).
- Miot, J. et al. Formation of single domain magnetite by green rust oxidation promoted by microbial anaerobic nitrate-dependent iron oxidation. Geochim. Cosmochim. Acta 139, 327–343 (2014).
- 48. Dunlop, D. J. Magnetite: Behavior near the single-domain threshold. *Science* **176**, 41–43 (1972).
- Levi, S. & Merrill, R. T. Properties of single-domain, pseudo-single-domain, and multidomain magnetite. *J. Geophys. Res. Solid Earth* 83, 309–323 (1978).
- Özdemir, Ö & Banerjee, S. K. A preliminary magnetic study of soil samples from west-central Minnesota. *Earth Planet. Sci. Lett.* 59, 393–403 (1982).
- Muxworthy, A. R. & Dunlop, D. J. First-order reversal curve (FORC) diagrams for pseudo-single-domain magnetites at high temperature. *Earth Planet. Sci. Lett.* 203, 369–382 (2002).
- Carvallo, C. & Muxworthy, A. Low-temperature first-order reversal curve (FORC) diagrams for synthetic and natural samples. *Geochem. Geophys. Geosyst.* 7 (2006).
- Lowenstam, H. A. Magnetite in denticle capping in recent chitons (Polyplacophora). Geol. Soc. Am. Bull. 73, 435–438 (1962).
- Bellon, U. D., Williams, W., Trindade, R. I. F., Maldanis, L. & Galante, D. Primordial magnetotaxis in putative giant paleoproterozoic magnetofossils. *Proc. Natl. Acad. Sci. USA* 121, e2319148121 (2024).

- Pérez-Huerta, A. et al. Biogeochemical fingerprinting of magnetotactic bacterial magnetite. *Proc. Natl. Acad. Sci. USA* 119, e2203758119 (2022).
- Goris, B., van den Broek, W., Batenburg, K. J., Mezerji, H. H. & Bals, S. Electron tomography based on a total variation minimization reconstruction technique. *Ultramicroscopy* 113, 120–130 (2012).
- 57. Dragonfly 2022.2 [Computer software]. Comet Technologies Canada Inc., Montreal, Canada; software available at https://www.theobjects.com/dragonfly.
- Coreform Cubit (Version 2023.8) [Computer software]. Orem, UT: Coreform LLC. Retrieved from http://coreform.com.
- Ó Conbhuí, P. et al. MERRILL: micromagnetic Earth related robust interpreted language laboratory. *Geochem. Geophys. Geosyst* 19, 1080–1106 (2018).
- Ahrens, J., Geveci, B. & Law, C. ParaView: An end-user tool for large data visualization, in The Visualization Handbook, Hansen, C. D. & Johnson, C. R. Eds. (Elsevier, 2005), pp. 717–731.
- 61. Pei, Z. Electron tomography, micromagnetic simulation, and crystal plane analysis of giant magnetofossils. *Zenodo* https://doi.org/10.5281/zenodo.12796923 (2025).

Acknowledgements

This study utilized samples from the International Ocean Discovery Program (IODP). We acknowledge Thermo Fisher Scientific for providing access to and supporting the cryo-EM facilities at the Cambridge Pharmaceutical Consortium. We acknowledge Simon M. Fairclough for assistance in cryogenic electron tomography, Xu Tang for assistance in electron diffraction analysis using TEM at the IGGCAS, Hassan A. Sheikh, George R. Lewis, and Bassel Arnaout for assistance in tomography data processing, and Sergio Valencia for discussions on micromagnetic simulation results. L.C. acknowledges support from the National Natural Science Foundation of China grant 42330204. L.C. and R.J.H. also thank the funding from the Royal Society Newton Advanced Fellowship (NAF \R1\201096). W.W. acknowledge Natural Environment Research Council (NERC) for their financial support (NE/Z000068/1, NE/W006707/1 and NE/ V001388/1). We thank Jinhua Li and an anonymous reviewer for their valuable suggestions and the editors for their efficient handling of our manuscript.

Author contributions

L.C. and R.J.H. designed research; Z.P., E.R., L.C., R.J.H., P.X., and W.W. performed research; Z.P., L.C., R.J.H., and W.W. contributed new analytic tools; Z.P. analyzed data; Z.P., E.R., L.C., R.J.H., P.X., and W.W. wrote the paper.

Competing interests

The authors declare no competing interests.

Additional information

Supplementary information The online version contains supplementary material available at https://doi.org/10.1038/s43247-025-02396-w.

Correspondence and requests for materials should be addressed to Liao Chang.

Peer review information Communications Earth & Environment thanks Jin-Hua Li and the other anonymous reviewer(s) for their contribution to the peer review of this work. Primary Handling Editors: Brittany Cymes and Carolina Ortiz Guerrero. [A peer review file is available].

Reprints and permissions information is available at http://www.nature.com/reprints

Publisher's note Springer Nature remains neutral with regard to jurisdictional claims in published maps and institutional affiliations.

Open Access This article is licensed under a Creative Commons Attribution-NonCommercial-NoDerivatives 4.0 International License, which permits any non-commercial use, sharing, distribution and reproduction in any medium or format, as long as you give appropriate credit to the original author(s) and the source, provide a link to the Creative Commons licence, and indicate if you modified the licensed material. You do not have permission under this licence to share adapted material derived from this article or parts of it. The images or other third party material in this article are included in the article's Creative Commons licence, unless indicated otherwise in a credit line to the material. If material is not included in the article's Creative Commons licence and your intended use is not permitted by statutory regulation or exceeds the permitted use, you will need to obtain permission directly from the copyright holder. To view a copy of this licence, visit http://creativecommons.org/licenses/by-nc-nd/4.0/.

© The Author(s) 2025